東北大学機関リポジトリ
TOUR
Tohoku University Repository

Effect of dust size and structure on scattered-light images of protoplanetary discs

著者	Ryo Tazaki, H Tanaka, T Muto, A Kataoka, S Okuzumi
journal or publication title	Monthly Notices of the Royal Astronomical Society
volume	485
number	4
page range	4951-4966
year	2019-03-08
URL	http://hdl.handle.net/10097/00128251

doi: 10.1093/mnras/stz662

Monthly Notices
of the
ROYAL ASTRONOMICAL SOCIETY

MNRAS **485,** 4951–4966 (2019)
Advance Access publication 2019 March 08

doi:10.1093/mnras/stz662

Effect of dust size and structure on scattered-light images of protoplanetary discs

Ryo Tazaki [1]★ H. Tanaka,[1] T. Muto,[2] A. Kataoka [3] and S. Okuzumi[4]

[1]*Astronomical Institute, Graduate School of Science, Tohoku University, 6-3 Aramaki, Aoba-ku, Sendai 980-8578, Japan*
[2]*Division of Liberal Arts, Kogakuin University, 1-24-2 Nishi-Shinjuku, Shinjuku-ku, Tokyo 163-8677, Japan*
[3]*National Astronomical Observatory of Japan, Mitaka, Tokyo 181-8588, Japan*
[4]*Department of Earth and Planetary Sciences, Tokyo Institute of Technology, Meguro, Tokyo 152-8551, Japan*

Accepted 2019 March 4. Received 2019 February 28; in original form 2018 December 1

ABSTRACT

We study scattered-light properties of protoplanetary discs at near-infrared wavelengths for various dust size and structure by performing radiative transfer simulations. We show that different dust structures might be probed by measuring disc polarization fraction as long as the dust radius is larger than the wavelength. When the radius is larger than observing wavelength, disc scattered light will be highly polarized for highly porous dust aggregates, whereas more compact dust structure tends to show low polarization fraction. Next, roles of monomer radius and fractal dimension for scattered-light colours are studied. We find that, outside the Rayleigh regime, as fractal dimension or monomer radius increases, colours of the effective albedo at near-infrared wavelengths vary from blue to red. Our results imply that discs showing grey or slightly blue colours and high polarization fraction in near-infrared wavelengths might be explained by the presence of large porous aggregates containing sub-micron-sized monomers.

Key words: radiative transfer – protoplanetary discs – infrared: ISM.

1 INTRODUCTION

The first step of planet formation is coagulation of dust particles in protoplanetary discs. Initial growth of dust particles yields fractal dust aggregates, whose porosity is higher than 99 per cent (Kempf, Pfalzner & Henning 1999; Ormel, Spaans & Tielens 2007; Okuzumi et al. 2012). According to grain growth studies, porosity of an aggregate in discs is a matter of debates; some studies suggest high porosity ($>$ 85 per cent) (e.g. Suyama, Wada & Tanaka 2008; Wada et al. 2008), whereas others predict lower porosity (67 $-$ 85 per cent) (e.g. Blum et al. 2006). In our Solar system, both fractal aggregates and compact particles are found, e.g. in comet 67P/Churyumov-Gerasimenko (Fulle et al. 2015, 2016; Bentley et al. 2016; Mannel et al. 2016). In a debris disc, the presence of mildly porous particles (porosity of about 60 per cent) is suggested by observations (e.g. Augereau et al. 1999). However, porosity of dust aggregates in a protoplanetary disc is still not clear observationally. Since dust porosity is a key to overcome bouncing barrier (Wada et al. 2011; Kothe et al. 2013; Brisset et al. 2017) and radial drift barrier (Okuzumi et al. 2012; Kataoka et al. 2013) in dust growth, characterization of dust porosity from disc observations may shed light on dust evolution in discs.

Since light-scattering properties sensitively depend on size, structure, and composition of dust particles (e.g. Kimura, Kolokolova & Mann 2006; Shen, Draine & Johnson 2008, 2009; Tazaki et al. 2016 (Paper I); Tazaki & Tanaka 2018 (Paper II); Halder, Deb Roy & Das 2018; Ysard et al. 2018), disc scattered light may provide information of dust properties. Since disc scattered light has been commonly detected in optical- and near-infrared wavelengths, in this study, we investigate a connection between dust properties and near-infrared disc scattered light.

Observed disc scattered-light colours are thought to reflect wavelength dependence of the albedo of dust particles (e.g. Mulders et al. 2013). In near-infrared wavelengths, most protoplanetary discs show grey colours in total intensity (e.g. Fukagawa et al. 2010), though some discs have reddish colours (e.g. Mulders et al. 2013; Long et al. 2017). More recently, Avenhaus et al. (2018) found that discs around T-Tauri stars have almost grey colours in polarized intensity.

The relation between radii of compact spherical grains and disc colours has so far been studied (e.g. Mulders et al. 2013). Although Min et al. (2012) and Kirchschlager & Wolf (2014) studied how dust structure and grain porosity affect disc scattered light, respectively, these studies did not investigate colours. Hence, a role of dust structure on disc colours has not yet been clarified well. Furthermore, Min et al. (2012) adopted the effective medium theory to compute optical properties of fluffy aggregates; however, once EMT is applied to fluffy aggregates, it significantly overestimates the degree of forward scattering (Paper I; Paper II). Hence, more accurate opacity model should be used. Kirchschlager & Wolf

★ E-mail: rtazaki@astr.tohoku.ac.jp

© 2019 The Author(s)
Published by Oxford University Press on behalf of the Royal Astronomical Society

Downloaded from https://academic.oup.com/mnras/article-abstract/485/4/4951/5372459 by Bungaku-Bu Library user on 20 May 2020

(2014) properly treated optical properties of porous grains; however, they only considered grain porosity up to 60 per cent, whereas fluffy dust aggregates that may form in discs have much higher porosity, e.g. more than 99 per cent (e.g. Kataoka et al. 2013).

An aim of this study is to examine a relation between disc scattered-light (total intensity, polarized intensity, and colours) and dust properties (size and structure). As a dust model, we particularly focus on highly porous dust aggregates (porosity higher than 85 per cent), whose presence has been suggested by grain growth models (Kempf et al. 1999; Ormel et al. 2007; Okuzumi et al. 2012). Disc scattered-light images are obtained by performing 3D Monte Carlo radiative transfer simulations and optical properties of porous aggregates are obtained by using a rigorous numerical method, the T-Matrix Method (Mackowski & Mishchenko 1996), or a carefully tested approximate method (Paper I; Paper II).

This paper is organized as follows. We first explain, in Section 2, our star and disc models used in this paper. We also summarize dust particle models and their optical properties. Then, we perform radiative transfer simulations of protoplanetary discs at near-infrared wavelengths and discuss images (Section 3) and disc scattered-light colours (Section 4). In Section 5, we study scattering properties of dust aggregates with various structure. Finally, we compare our results with disc observations and close with a Conclusion section.

2 MODELS

2.1 Star and disc model

The central star is assumed to be a T-Tauri star with the effective temperature of 4000 K and the radius of $2R_\odot$. The dust surface density is assumed to be the single power-law distribution, $\Sigma_d = \Sigma_0 (R/R_{\rm out})^{-1}$, where R is the distance from the central star, and Σ_0 is the surface density of dust grains at the outer radius $R_{\rm out}$. The disc inner and outer radii are truncated at 10 and 100 au, respectively. The total dust disc mass is set as $10^{-4}M_\odot$. All simulations shown in this paper has the same total dust disc mass. The vertical distribution of dust grains is assumed to be the Gaussian distribution with the dust scale height of $H_d = 3.3 \times 10^{-2} (R/1\,{\rm au})^\beta$ au. In this paper, we consider a flared disc geometry with $\beta = 1.25$ (Kenyon & Hartmann 1987). In Section 4.3, we address how the choice of disc geometry affects our conclusion.

We perform radiative transfer simulations using a 3D Monte Carlo radiative transfer code, RADMC-3D (Dullemond et al. 2012). The radial mesh is uniformly spaced in a logarithmic space of [5,105] au with 256 grids. The zenith and azimuthal angles are uniformly spaced in a linear space of $[2\pi/9, 7\pi/9]$ and $[0, 2\pi]$ with 128 and 256 grids, respectively. The number of photon packages for the scattering Monte Carlo simulation is 10^9. In this paper, we consider three near-infrared wavelengths: $\lambda = 1.1\,\mu$m, $1.6\,\mu$m, and $2.2\,\mu$m.

2.2 Dust models and methods

To study how size and internal structure of dust particles affect observational appearance of discs, we consider three types of dust models. In this paper, we basically use the term *large* or *small* dust radius when the radius is large or small *compared to* $\lambda/(2\pi)$, where λ is a wavelength of interest.

(i) *Single monomer model*: 0.1-μm-sized homogeneous spherical grain (= a monomer particle). This particle is used to form porous dust aggregates described below. Optical properties of the monomer are obtained by using the Mie theory (Bohren & Huffman 1983). The monomer radius assumed is roughly the same as the constituent particle of cometary dust aggregates (e.g. Kimura et al. 2006). Since we assume that a monomer is homogeneous spherical grain, volume filling factor of the monomer is unity.

(ii) *Porous dust aggregate model*: We consider two types of fractal dust aggregates, ballistic cluster cluster agglomerate (BCCA) and ballistic particle cluster agglomerate (BPCA) (see Fig. 1). Fractal dust aggregates obey a relation $N = k_0 (R_{\rm g}/R_0)^{d_{\rm f}}$, where N is the number of monomers, $R_{\rm g}$ is the radius of gyration of the aggregate, R_0 is the radius of a monomer, k_0 is the fractal prefactor, and $d_{\rm f}$ is the fractal dimension. Typically, BCCA and BPCA have fractal dimension and fractal prefactor $d_{\rm f} = 1.9$ and $k_0 = 1.04$ and $d_{\rm f} = 3.0$ and $k_0 = 0.3$, respectively (Paper I). It is convenient to define the characteristic radius by $R_{\rm c} = \sqrt{5/3} R_{\rm g}$ (Mukai et al. 1992).[1] In this paper, volume filling factor of the aggregate is defined by $f = N R_0^3 / R_{\rm c}^3$ (Mukai et al. 1992).[2] In addition, it is also useful to define volume-equivalent radius $R_{\rm V} \equiv R_0 N^{1/3} = R_{\rm c} f^{1/3}$. Porosity of dust aggregates can be defined by $P = 1 - f$. If the volume filling factor is unity, the characteristic radius is equal to the volume equivalent radius.

Optical properties of the BCCA and BPCA models are obtained by using a rigorous numerical method, T-Matrix Method [3] (TMM; Mackowski & Mishchenko 1996) with the Quasi-Monte Carlo orientation averaging method (Okada 2008).[4] We also use the modified mean field theory (MMF) developed in Paper II.[5]

We are mainly interested in porous dust aggregates whose radii are larger than $\lambda/(2\pi)$ because small aggregates simply give rise to Rayleigh scattering. For TMM computation, we adopt $N = 1024$. Although $N = 1024$ is not a large number, for $R_0 = 0.1\,\mu$m, the characteristic radii of the BCCA and BPCA models are $R_{\rm c} = 4.8\,\mu$m and $1.9\,\mu$m, respectively; thus, the characteristic radii exceed $\lambda/(2\pi)$ when λ corresponds to near-infrared wavelengths. Porosity of the BCCA and BPCA models is 99 per cent and 85 per cent, respectively. For further large aggregates, TMM computation becomes time-consuming, and hence we use MMF instead of TMM. Comparison between MMF and TMM is available in Paper I, Paper II, and Appendix A.

(iii) *Compact dust aggregate model*: Single-sized compact dust aggregate, whose porosity is low enough so that the distribution of

[1] The solid sphere of the radius a has the radius of gyration $R_{\rm g} = \sqrt{3/5} a$. Thus, characteristic radius of porous aggregate with the radius of gyration $R_{\rm g}$ is defined in this way.

[2] A way to define filling factor is not unique, and the choice may somewhat affect porosity values, in particular for BCCA. Our definition of filling factor has been widely used (e.g. Mukai et al. 1992), and hence, in this paper, we follow this conventional definition.

[3] The code is available at ftp://ftp.eng.auburn.edu/pub/dmckwski/scatcodes/. A newer version of this code is available at http://www.eng.auburn.edu/~dmckwski/scatcodes/.

[4] More detailed information about TMM calculations of porous dust aggregate model is available in Paper I and Paper II.

[5] The Rayleigh–Gans–Debye theory studied in Paper I is a single scattering theory, whereas multiple scattering is often important for relatively large compact aggregates with $d_{\rm f} > 2$. A simple way to implement multiple scattering is to adopt the mean field approximation (Berry & Percival 1986; Botet, Rannou & Cabane 1997), although the mean field approximation fails to predict the single scattering albedo, once multiple scattering inside the aggregate becomes dominant (Paper II). Paper II proposed the modified mean field theory in which inaccurate behaviours in the mean field theory are improved by employing geometrical optics approximation (e.g. Bohren & Huffman 1983).

Downloaded from https://academic.oup.com/mnras/article-abstract/485/4/4951/5372459 by Bungaku-Bu Library user on 20 May 2020

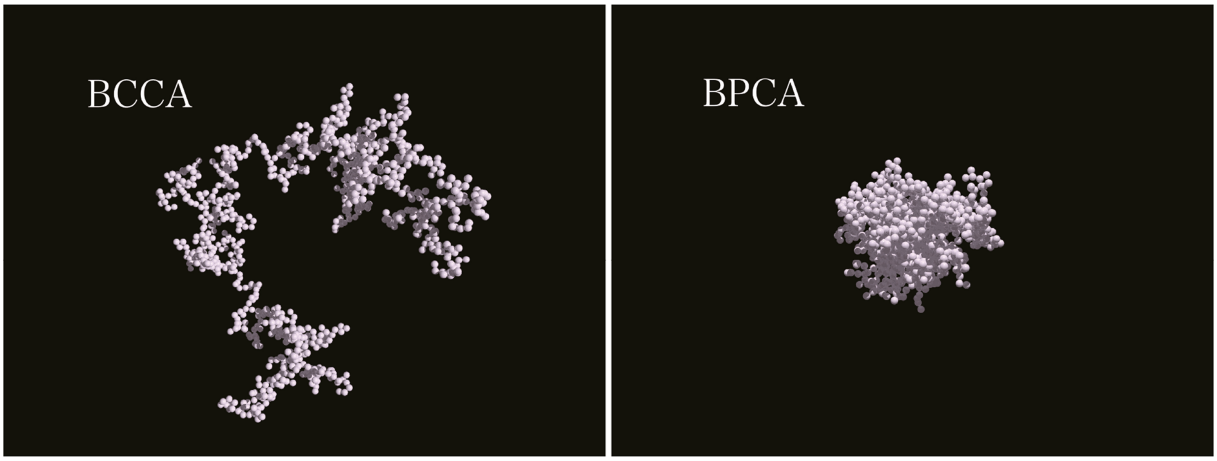

Figure 1. Morphology of porous dust aggregates. Left- and right-hand panels correspond to the BCCA and BPCA models, respectively. The number of monomers is 1024 and the monomer radius is set as $R_0 = 0.1\,\mu$m, and hence the characteristic radii of the BCCA and BPCA models are $R_c = 4.8\,\mu$m and $1.9\,\mu$m, respectively. Both dust aggregates have the same volume equivalent radius $R_V \simeq 1\,\mu$m. Hence, BCCA and BPCA have porosity of 99 per cent and 85 per cent, respectively.

hollow spheres[6] (DHS; Min, Hovenier & de Koter 2005; Min et al. 2016) can be applicable outside the Rayleigh domain. We adopt the irregularity parameter $f_{max} = 0.8$ (Min et al. 2016). The volume equivalent radius of a compact dust aggregate is varied from $0.1\,\mu$m to $5.0\,\mu$m. In the DHS method, volume filling factor of an aggregate is not necessary to be specified.

Among three dust models, we adopt astronomical silicate for the optical constant (Draine & Lee 1984; Laor & Draine 1993). In this case, opacities and scattering matrix elements of the BCCA and BPCA models have already been presented in Paper I and Paper II. We discuss the effect of dust composition (Section 4.3) and monomer radius and fractal dimension (Section 5) in more detail.

2.3 Optical properties of out dust models

We compute optical properties of dust models given in Section 2.2. Fig. 2 shows dust optical properties at wavelength $\lambda = 1.6\,\mu$m for the single monomer model, the porous dust aggregate model (the BCCA and BPCA models with $N = 1024$ and $R_0 = 0.1\,\mu$m), and the compact dust aggregate model ($R_V = 1\,\mu$m). Since BCCA and BPCA have $N = 1024$ and $R_0 = 0.1\,\mu$m, their volume equivalent radii are $R_V = R_0 N^{1/3} \simeq 1.0\,\mu$m. Therefore, BCCA, BPCA and compact dust aggregates have the same volume equivalent radii.

In this paper, scattering matrix elements are defined by $Z_{ij} = S_{ij}/(k^2 m_{dust})$, where S_{ij} is those defined by Bohren & Huffman (1983), k is the wavenumber, and m_{dust} is the mass of dust particle. Since Z_{11} is a differential cross-section per unit mass, it is related to the scattering opacity κ_{sca} via

$$\kappa_{sca} = \oint Z_{11} d\Omega, \tag{1}$$

where $d\Omega$ is the solid angle. For the sake of simplicity, in this paper, we refer Z_{11} as a *phase function*. As shown in Fig. 2, scattering is anisotropic for BCCA, BPCA, and compact dust aggregate models. This is because these aggregates have the radii larger than $\lambda/(2\pi)$. On the other hand, the monomer model shows isotropic scattering due to Rayleigh scattering.

The degree of linear polarization is given by $-Z_{12}/Z_{11}$. For small particles, such as a monomer particle, the degree of polarization is 100 per cent at 90 deg scattering angle due to Rayleigh scattering. On the other hand, for a particle larger than $\lambda/(2\pi)$, the degree of polarization depends on the structure of dust aggregates. Porous dust aggregates tend to show high degree of polarization with a bell-shaped profile (Fig. 2). This is because multiple scattering inside the aggregate is suppressed due to its highly porous structure, and then, polarization properties are determined by those of the monomer (see equation 9 in Paper I). The degree of polarization of compact dust aggregates is lower than that of porous dust aggregates due to occurrence of multiple scattering inside the particle. Hence, the degree of polarization provides valuable information about structure of dust aggregates when the particle radius is larger than wavelength.

3 RESULTS OF RADIATIVE TRANSFER SIMULATIONS: IMAGES

We perform radiative transfer simulations using a model described in Section 2. Optical properties used in the simulations are the ones summarized in Section 2.3.

Total intensity images (middle panels of Fig. 3) can be used as a diagnostics of particle radius. Both the porous and compact aggregate models show the brightness asymmetry, that is, the near side of the disc is brighter than the backward side. This is because the dust particle radii assumed are larger than the wavelength (radius $\gtrsim \lambda/2\pi$), and hence strong forward scattering occurs. Meanwhile, for the single monomer model, the brightness asymmetry is weak because the monomer is a Rayleigh scatterer, that is, isotropic scattering occurs.

Although differences between porous aggregates (BCCA and BPCA) and compact aggregates are less obvious in total intensity images, they clearly differ in images of polarization fraction. Fig. 4 shows polarization fraction measured at $R = 50$ au from Fig. 3, where scattering angles are estimated by using a scattered-light mapping method (Stolker et al. 2016). As shown in Fig. 4, the polarization fraction of the BCCA and BPCA models is as high as 65–75 per cent. Polarization fraction obtained by simulations is

[6]In order to avoid strong resonances appeared in scattering properties, we prefer to use the DHS method rather than the Mie theory for compact particles larger than $\lambda/(2\pi)$.

Downloaded from https://academic.oup.com/mnras/article-abstract/485/4/4951/5372459 by Bungaku-Bu Library user on 20 May 2020

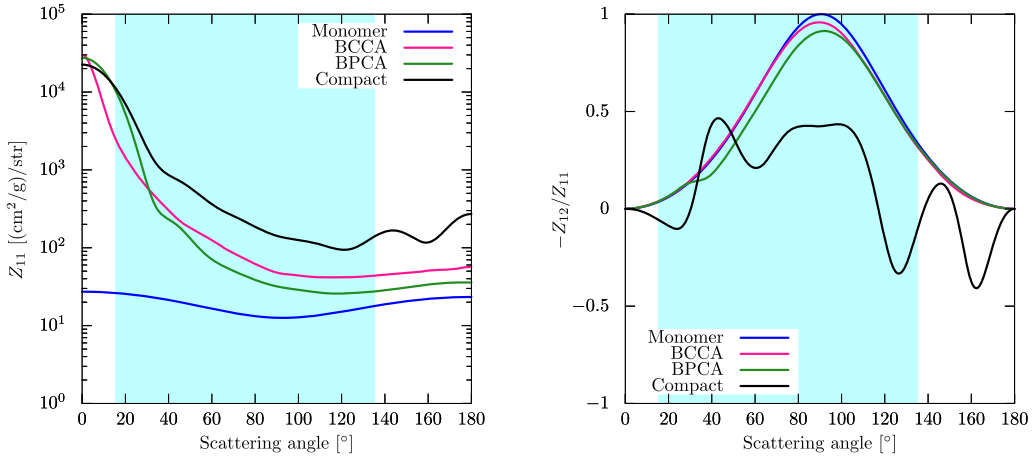

Figure 2. Phase function Z_{11} (left) and the degree of linear polarization $-Z_{12}/Z_{11}$ (right). Optical properties of the single-monomer model, the BCCA and BPCA models, and the compact dust aggregate model are obtained by using the Mie theory, TMM, and DHS, respectively. A single monomer has the radius of 0.1 μm, whereas the porous (BCCAs and BPCAs) and compact dust aggregate models have the same volume equivalent radii 1.0 μm. Wavelength is set as $\lambda = 1.6\,\mu$m. Hatched region indicates a range of scattering angle to be observed for a disc with the flaring index $\beta = 1.25$ and the inclination angle $i = 60^\circ$.

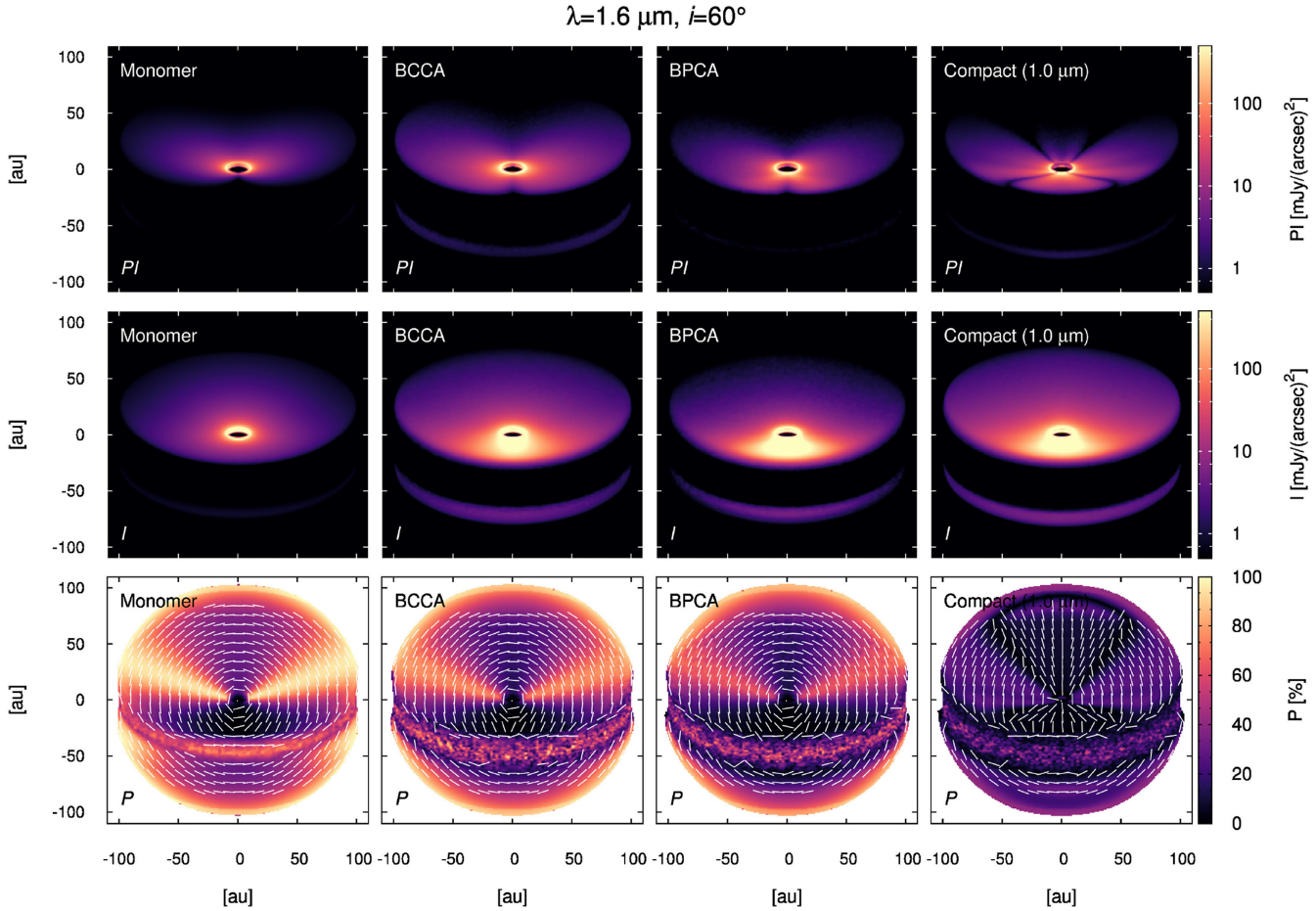

Figure 3. Polarized intensity (top), total intensity (middle), and polarization fraction (bottom). From left to right, each panel indicates the results for the single monomer model (0.1-μm-sized spherical particles), the BCCA and BPCA models ($N = 1024$, $R_0 = 0.1\,\mu$m, astronomical silicate), and the compact dust aggregate model with the radius of 1.0 μm. The wavelength is $\lambda = 1.6\,\mu$m and the inclination angle is $i = 60^\circ$. Optical properties of BCCAs and BPCAs are calculated by a rigorous method, TMM. No star is included in images (perfect coronagraph). For the porous dust aggregate models, the disc shows brightness intensity asymmetry (in total intensity) due to forward scattering as well as high polarization fraction.

Downloaded from https://academic.oup.com/mnras/article-abstract/485/4/4951/5372459 by Bungaku-Bu Library user on 20 May 2020

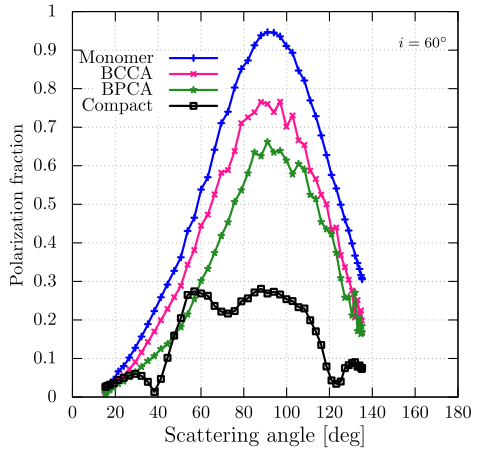

Figure 4. Polarization fraction as a function of scattering angles at $R = 50$ au measured from simulated images in Fig. 3. Because of multiple scattering at the disc surface, polarization fraction is smaller than the degree of polarization given in Fig. 2 (right).

Table 1. Disc integrated polarization fraction at $\lambda = 1.6\,\mu$m for the our dust models.

Inclination angle	Monomer	BCCA	BPCA	Compact
$i = 0°$	84%	63%	46%	22%
$i = 15°$	80%	57%	42%	19%
$i = 30°$	68%	46%	31%	21%
$i = 45°$	53%	32%	19%	13%
$i = 60°$	42%	18%	8%	8%
$i = 75°$	37%	14%	8%	6%

somewhat smaller than the degree of polarization (Fig. 2). This is mainly due to occurrence of multiple scattering at the disc surface because the disc is optically thick. When we compare Figs 2 and 4, it is found that the degree of polarization is similar between the monomer, the BCCA and BPCA models, whereas highest polarization fraction observed in the discs for these particles can largely differ.

Polarization fraction of the compact dust aggregate model can be much smaller than those of porous dust aggregate models. This is because multiple scattering easily occurs for more compact structure of dust aggregates once the aggregate radius becomes larger than $\lambda/2\pi$.[7] As a result, compact dust aggregates show lower polarization fraction compared to the porous dust aggregates.

Table 1 summarizes integrated polarization fraction of discs for various dust models. For all dust models, more inclined discs show lower polarization fraction because wider scattering angles can be observed. The BCCA model predicts that integrated polarization fraction is as high as 63 per cent for a face-on disc, whereas it is only 14 per cent for a very inclined disc ($i = 75°$). On the other hand, more compact dust structure, like BPCA and compact dust models, results in smaller integrated polarization fraction than those of BCCA. As a result, it is found that disc polarization fraction is an important quantity to distinguish different dust structure, where relatively high polarization fraction of BCCA and monomer could be distinguished by the presence of forward scattered light in total intensity image.

The tendency that porous aggregates show high polarization fraction is compatible with the previous works by Min et al. (2012), who used EMT, and by Kirchschlager & Wolf (2014), who adopted less porous particle models. However, as shown in Appendix A, EMT largely under-/overestimate the scattered-light intensity and the polarization fraction for large fluffy dust aggregates. This is due to the fact that phase function obtained by EMT shows extremely strong forward scattering, which suppresses both large-angle scattering (reducing total intensity) and multiple scattering at disc surface (increasing polarization fraction).

Polarized intensity does not show clear brightness asymmetry because polarization fraction becomes small along the minor axis. The compact dust aggregate model shows some slits in the image of polarized intensity. In our compact dust aggregate model, oscillatory behaviour appears in the angular profile of the degree of polarization due to resonances arising from smooth spherical surfaces (see Fig. 2). However, realistic compact dust aggregates are thought to have surface roughness, and hence these resonances would be smeared out (e.g. Min et al. 2016). Therefore, these slits in the image thought to be unrealistic. The reason why a monomer particle, which also has smooth surface, does not show the oscillatory behaviour is simply that Rayleigh scattering occurs, that is, scattering is coherent. It is also worth mentioning that even if the oscillatory behaviour is suppressed, polarization flip at disc backward side may remain for some dust properties because of the effect called negative polarization branch (e.g. Kirchschlager & Wolf 2014). This effect, for example, has been observed for cometary dust particles (e.g. Kolokolova et al. 2007).

4 RESULTS OF RADIATIVE TRANSFER SIMULATIONS: SCATTERED-LIGHT COLOURS

We define the scattered-light colour by

$$\eta = \frac{\log(L_{\mathrm{disc},\lambda_2}/L_{\mathrm{star},\lambda_2}) - \log(L_{\mathrm{disc},\lambda_1}/L_{\mathrm{star},\lambda_1})}{\log(\lambda_2/\lambda_1)}, \quad (2)$$

where $L_{\mathrm{disc},\,\lambda}$ and $L_{\mathrm{star},\,\lambda}$ are total luminosity of disc and central star, respectively, for either total intensity or polarized intensity. We adopt $\lambda_1 = 1.1\,\mu$m and $\lambda_2 = 2.2\,\mu$m. In this paper, we classify scattered-light colours into blue, grey, and red when $\eta < -0.5$, $-0.5 \leq \eta \leq 0.5$, and $\eta > 0.5$, respectively.

4.1 Comapct aggregates versus porous dust aggregates

Fig. 5 and Table 2 show scattered-light colour for both in total intensity (η_{I}) and in polarized intensity (η_{PI}) at inclination angle $i = 60°$. Fig. 5 also compares total intensity colours of BCCA ($R_{\mathrm{c}} = 4.8\,\mu$m) to those of the compact aggregate with the same radius. We find that total intensity colours of BCCA ($R_{\mathrm{c}} = 4.8\,\mu$m) are grey or slightly blue for both total and polarized intensity. Meanwhile, a compact aggregate with $R_{\mathrm{V}} = 4.8\,\mu$m shows reddish colour (Mulders et al. 2013). BPCA ($R_{\mathrm{c}} = 1.9\,\mu$m) also show grey colours in total intensity, whereas compact aggregates with 1.9 μm show reddish colours. As a result, porous aggregates large compared to wavelength tends to show grey or slightly blue colours in total intensity, whereas large compact aggregates give rise to reddish colours. Therefore, even if porous and compact dust aggregates have the same radii, their scattered-light colour can differ. It is worth mentioning that for compact dust aggregates, grey colours

[7] When the particle has refractive index close to unity, polarization fraction remains high even if the size parameter exceeds unity (see e.g. chapter 6 of Bohren & Huffman 1983). This is due to multiple scattering inside the sphere becomes sub-dominant for such a transparent material.

Downloaded from https://academic.oup.com/mnras/article-abstract/485/4/4951/5372459 by Bungaku-Bu Library user on 20 May 2020

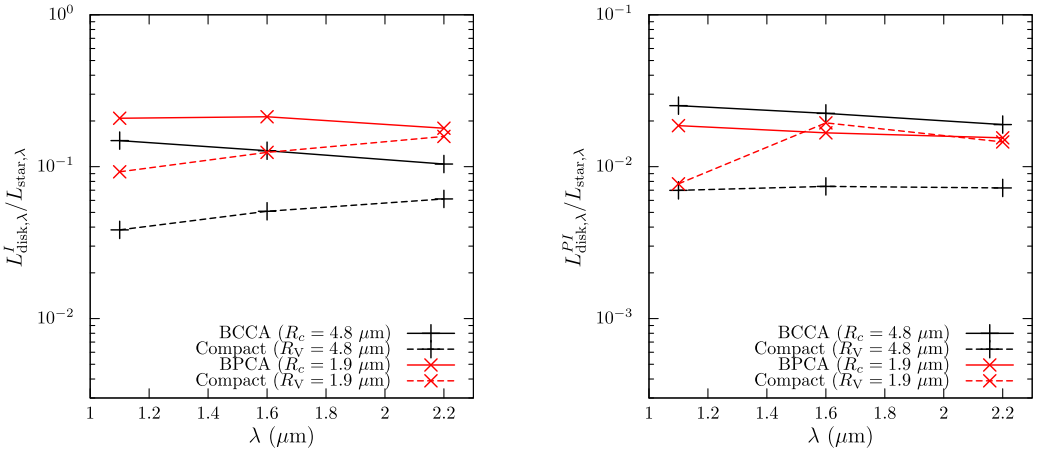

Figure 5. Fractional luminosity in total intensity (left) and polarized intensity (right) at the inclination angle $i = 60°$. Black and red solid lines represent the results for BCCA and BPCA, respectively. Black and red dashed lines indicate the results for compact dust aggregates with 4.8 μm and 1.9 μm radii, respectively.

Table 2. Disc scattered-light colour for different aggregate models.

Dust model	$\eta_{\rm I}$	$\eta_{\rm PI}$
Monomer	− 2.4	− 2.4
BCCA ($r_V = 1.0\,\mu$m, $R_c = 4.8\,\mu$m)	− 0.51	− 0.41
BPCA ($r_V = 1.0\,\mu$m, $R_c = 1.9\,\mu$m)	− 0.21	− 0.27
Compact ($R_V = 1.0\,\mu$m)	0.030	0.099
Compact ($R_V = 1.9\,\mu$m)	0.77	0.91
Compact ($R_V = 4.8\,\mu$m)	0.68	0.053

can appear when the radius is comparable to the wavelength (see Fig. B4 in Appendix B for more detail).

4.2 Scattered-light colours of millimetre-sized BCCA

Due to strong aerodynamic coupling, highly porous dust aggregates at disc surface may be much larger than micron-size, whereas large compact dust aggregates are likely to settle down to the midplane. In Section 4.1, we concluded that a few micron-sized BCCA are shown to yield grey or slightly blue rather than reddish colours. However, one may doubt that the presence of further larger fluffy aggregates than those considered in Section 4.1 may makes the disc reddish. In this section, we show that colours remain almost the same even if the radius of aggregates is increased to millimetre-size.

4.2.1 Phase function

Since we are interested in aerodynamically coupled aggregates, we consider BCCA, whose mass-to-area ratio is the same as the individual monomer particle. In particular, we study scattering properties of BCCA with radius from $R_c = 1\,\mu$m to 1 mm. Millimetre-sized BCCA with $R_0 = 0.1\,\mu$m contains $\sim 10^7$ monomers, and hence, TMM computation is time consuming. Thus, we adopt MMF instead of TMM. For MMF, angular dependence of phase matrix elements is reliably computed when the single scattering assumption is validated (Paper II):

$$\Delta\phi < 1, \tag{3}$$

$$|m - 1| < 2, \tag{4}$$

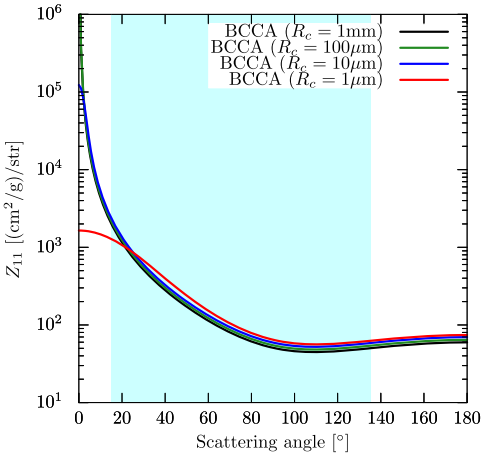

Figure 6. Phase function Z_{11} of extremely large BCCA obtained by MMF. The wavelength is set as $\lambda = 1.6\,\mu$m. Hatched region indicates a range of scattering angle to be observed for a disc with the flaring index $\beta = 1.25$ and the inclination angle $i = 60°$.

where $\Delta\phi$ is the (maximum) phase shift of dust aggregates and m is the complex refractive index. For astronomical silicate, the first condition is satisfied for $\lambda \geq 0.85\,\mu$m for BCCA with $R_0 = 0.1\,\mu$m. It should be emphasized that in the case of BCCA, $\Delta\phi$ does not depend on the aggregate radius. In optical and near-infrared wavelengths, the second condition is also satisfied (see fig. 3 in Paper I).

Fig. 6 shows phase function Z_{11} of BCCA with radius from $R_c = 1\,\mu$m to 1 mm obtained by MMF. As the aggregate radius increases, forward scattering becomes strong; however, intermediate- and backward-scattered intensity saturates. This saturation is a natural consequence of single scattering by dust aggregates (Berry & Percival 1986; Paper I). Mechanism of the saturation is illustrated in Fig. 7. For large-angle scattering ($\theta \gtrsim (2\pi R_g/\lambda)^{-1}$), scattered intensity is dominated by coherent scattered waves from a pair of monomers separated by the distance smaller than the aggregate radius. On the other hand, a pair of monomers with separation as large as aggregate radius only gives rise to incoherent contribution to the scattered intensity because their optical path of difference is large. Thus, scattered intensity at large scattering angles is

Downloaded from https://academic.oup.com/mnras/article-abstract/485/4/4951/5372459 by Bungaku-Bu Library user on 20 May 2020

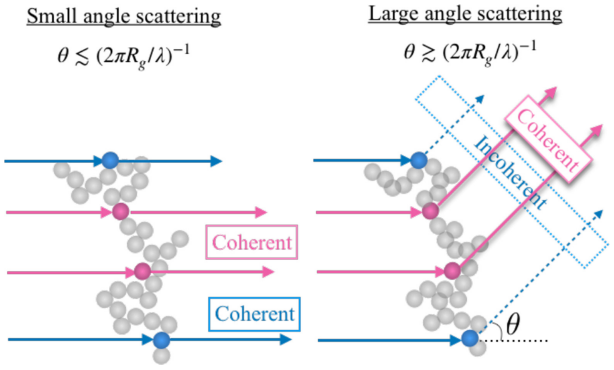

Figure 7. Schematic illustration to explain saturation of Z_{11} for large-angle scattering. At large scattering angles, scattered light is dominated by coherent light scattered from small-scale structure of the aggregate, whereas large-scale structure, e.g. aggregate radius, only produces incoherent light due to relatively large optical path of difference. Hence, the aggregate radius is insensitive to Z_{11} at intermediate scattering angles.

governed by its small-scale structure, e.g. fractal dimension and the monomer's properties, rather than the aggregate radius. As a result, phase function Z_{11} shown in Fig. 6 is insensitive to the characteristic radius at intermediate- and back-scattering angles. For the case of small-angle scattering ($\theta \lesssim (2\pi R_g/\lambda)^{-1}$), large-scale structure of aggregates can produce coherent scattered light, and therefore, Z_{11} depends on the aggregate radius as can be seen in Fig. 6.

4.2.2 *Disc scattered-light colours*

By using optical properties of BCCA computed in Section 4.2.1, we perform radiative transfer simulations of discs. As shown in Fig. 6, millimetre-sized BCCAs show very sharp and intense forward scattering. Hence, a large number of grids will be required in the radiative transfer calculation.[8] In addition, a sharp increase of phase function makes opacity integration inaccurate. In order to avoid these problems, we place an upper limit on peaking forward scattering, since forward scattering outside the observable angle range is not likely to affect observed images. In this paper, we adopt $Z_{11}(\theta < \theta_c) = Z_{11}(\theta_c)$, where θ_c is taken to be 1 deg.

Fig. 8 shows results of radiative transfer simulations of discs containing BCCA with $R_c = 1\,\mu$m to 1 mm. (Obtained images are shown in Fig. A5.) It is found that the disc scattered light is insensitive to the characteristic radius of aggregate. This is because scattered-light intensity in a range of observable scattering angles does not depend on the characteristic radius (see the hatched range of scattering angles in Fig. 6). Table 3 shows that colours become shallower as the characteristic radius increases; however, even if the aggregate radius is increased up to millimetre size, colours do not reach the reddish colour regime. Colours of BCCA with $R_0 = 0.1\,\mu$m seem to be slightly blue, but not too blue like Rayleigh scattering particles (see Table 2). Therefore, even if the disc contains BCCA as large as millimetre size at the surface, reddish colour scattered light is not likely to occur.

In Fig. 6, we also investigate how the monomer radius affects disc scattered lights. In order to satisfy Equation (3), we consider millimetre-sized BCCA with $R_0 = 0.01$-μm-sized monomers. If the monomer radius is decreased, the disc becomes faint due to small albedo value of dust aggregates. Large BCCA of small monomers show bluer colours than those of $R_0 = 0.1\,\mu$m monomers. Therefore, scattered-light colours of BCCA depend on the monomer radius (see Section 5 for more detail).

[8]See also Section 6.5.6 in Manual for RADMC-3D Version 0.39, which is available at http://www.ita.uni-heidelberg.de/~dullemond/software/radmc-3d/download.html.

Table 3. Disc scattered-light colour for extremely large BCCA.

Aggregate tadius	η_I	η_{PI}
$R_c = 1\,\mu$m (MMF)	− 1.0	− 0.64
$R_c = 10\,\mu$m (MMF)	− 0.69	− 0.68
$R_c = 100\,\mu$m (MMF)	− 0.67	− 0.66
$R_c = 1$ mm (MMF)	− 0.58	− 0.58
$R_c = 1$ mm, $R_0 = 0.01\,\mu$m (MMF)	− 1.2	− 1.1
$R_c = 4.8\,\mu$m (TMM)	− 0.51	− 0.41
$R_c = 4.8\,\mu$m (MMF)	− 0.67	− 0.67

Finally, we mention error of scattered-light colours due to the use of MMF (see also Appendix A). MMF results show slightly blue colours for large BCCA; however, MMF tends to produce bluer colours compared to rigorous TMM calculations (see Table 3). For $R_c = 4.8\,\mu$m, the difference of the slope is $\Delta_I \equiv \eta_{I,\,TMM} - \eta_{I,\,MMF} \simeq 0.16$, where $\eta_{I,\,TMM}$ and $\eta_{I,\,MMF}$ are total intensity colours obtained by TMM and MMF, respectively. Similarly, we can define the difference of the slope for polarized intensity, $\Delta_{PI} \equiv \eta_{PI,\,TMM} - \eta_{PI,\,MMF} \simeq 0.26$. Hence, TMM results are shallower than MMF results (see Fig. A4). These differences are mainly due to approach of $\Delta\phi$ to unity, which makes MMF inaccurate due to occurrence of multiple scattering. $\Delta\phi$ increases as the wavelength decreases; however, for sufficiently large BCCA (e.g. $d_f \approx 2$), $\Delta\phi$ does not depend on the aggregate radius and depends only on the property of the monomer (refractive index and size parameter) (Berry & Percival 1986; Paper II). Hence, it is reasonable to assume that errors in slope for $R_c = 10\,\mu$m, $100\,\mu$m, and 1 mm are similar to those of $R_c = 4.8\mu$m, and therefore, slope of these large BCCA may be shallower than those given in Table 3 by $\Delta_I = 0.16$ and $\Delta_{PI} = 0.26$ for total intensity and polarized intensity, respectively. As a result, by considering errors in colours between TMM and MMF, millimetre-sized BCCA with $R_0 = 0.1\,\mu$m are thought not to produce reddish colours at near-infrared wavelengths and more likely to produce grey colours.

4.3 Effect of disc geometry, inclination, and dust composition

In Sections 4.1 and 4.2, we studied scattered-light colour by assuming a single disc geometry, inclination angle, and a single dust composition. Here, we address how these parameters affect scattered-light colours.

We vary the following parameters: flaring index β, disc inner and outer truncation radius R_{in} and R_{out}, respectively, inclination angle i, and dust composition. Total dust mass is kept the same, that is $10^{-4}M_\odot$. As a dust composition, we consider the carbon-rich composition, which is a mixture of silicate, iron sulphide, water ice, and amorphous carbon. Fraction of each ingredients is determined by a recipe given by Min et al. (2011) with the carbon partition parameter $w = 1$. Optical constants of silicate, iron sulphide, and water ice are taken from Henning & Stognienko (1996) and for amorphous carbon from Zubko et al. (1996). These optical constants are mixed by using the Bruggeman mixing rule (Bruggeman 1935). Optical properties of carbon-rich BCCA ($R_c = 4.8\,\mu$m and $R_0 = 0.1\,\mu$m) are obtained by using MMF.

Downloaded from https://academic.oup.com/mnras/article-abstract/485/4/4951/5372459 by Bungaku-Bu Library user on 20 May 2020

In Fig. 9, we show scattered-light colour of the BCCA model for various parameters. Table 4 summarizes scattered-light colours. It is shown that that these parameters affect mainly magnitude of fractal luminosity. Although colours can differ for different disc geometries and dust composition, within a parameter range we studied, these parameters do not significantly change our results given in Sections 4.1 and 4.2.

It should be mentioned that fractional luminosity in total intensity and polarized intensity derived in this paper is higher than the observed values (Fukagawa et al. 2010; Avenhaus et al. 2018). However, as shown in Fig. 9, disc scattered-light luminosity is sensitive to the disc structure and dust composition, although the colours are less sensitive to them. Hence, we expect observed fractional luminosity in total intensity and polarized intensity might be explained by including these effects, though we need to check it for each object. This is beyond the scope of this paper.

5 EFFECT OF DUST AGGREGATE STRUCTURE ON SCATTERING PROPERTY

In Section 4, it is shown that large porous dust aggregates show slightly blue or grey colours in scattered light, while large compact aggregates to show reddish colours. In this section, we discuss reasons for this by considering intrinsic optical properties of dust aggregates.

We define the effective albedo by $\omega_{\rm eff} = \kappa_{\rm sca}^{\rm eff}/(\kappa_{\rm abs} + \kappa_{\rm sca}^{\rm eff})$, where $\kappa_{\rm sca}^{\rm eff} = (1-g)\kappa_{\rm sca}$ is the effective scattering opacity, $\kappa_{\rm abs}$ is the absorption opacity, and g is the asymmetry parameter. Since small-angle scattered light is hardly observable, the effective albedo is a useful quantities (see also Dullemond & Natta 2003; Min et al. 2010; Mulders et al. 2013). In the case of efficient forward scattering ($g \sim 1$), only a small amount of incident photons will be scattered toward the observer (supposed to be at $\theta \neq 0$); hence, the effective albedo has small values. On the other hand, if scattering is isotropic ($g \sim 0$), the effective albedo gives rise to the single scattering albedo ω. Thus, the effective albedo might be used as a qualitative measure of disc scattered-light colours.

In order to obtain the effective albedo of dust aggregates, we use MMF developed by Paper II. In MMF, the structure of dust aggregates is specified in terms of two-point correlation function of monomers (Berry & Percival 1986; Botet et al. 1997; Paper II). In addition, by using mean field assumption, multiple scattering inside the aggregate is solved in a self-consistent manner. Hence, it is suitable to study how fractal dimension affects optical cross-sections

Fig. 10 shows the effective albedo for dust aggregates with various fractal dimension and monomer radii. It is found that when the characteristic radius is fixed to 2.5 μm, with increasing fractal dimension from 2 to 3, colours of the effective albedo vary from blue to red at near-infrared wavelengths.

This can be explained as follows. For large compact dust aggregates, as wavelength decreases, forward scattering becomes more efficient, that is, g increases. Thus, the effective albedo decreases for short-wavelength domain (Mulders et al. 2013). Hence, large compact aggregates show reddish colours. Meanwhile, for large highly porous aggregates, asymmetry parameter g becomes almost constant with respect to the wavelength due to saturation of scattered light (see Appendix C), and therefore, anisotropic scattering does not reduce the effective albedo. As a result, porous aggregates tend to show more bluer colours compared to compact aggregates.

Scattered-light colours depend also on the monomer radius, in particular for $d_{\rm f} = 2$ (like BCCA). In the right-hand panel of Fig. 10, we show the effective albedo of fluffy dust aggregates ($k_0 = 1.0$ and $d_{\rm f} = 2.0$) with various monomer radii, where the complex refractive index is set as $m = 1.67 + 0.0326i$ for the sake of simplicity (corresponding to astronomical silicate at $\lambda = 1.6\,\mu$m). It is found that when the monomer radius is much smaller than the NIR wavelength (cases of $R_0 = 1$ nm and 10 nm), NIR slope of the effective albedo is blue (see also Table 3). On the other hand, for the case of $R_0 = 1\,\mu$m, the single scattering assumption is violated, and hence, the effective albedo becomes red due to occurrence of multiple scattering inside the cluster. Thus, the monomer radius is sensitive to scattered-light colours of large fluffy dust aggregates.

There are three possibilities to explain observed grey scattered-light colours. One possibility is moderately compressed aggregates. As shown in Fig. 10, scattered-light colours of aggregates with $d_{\rm f} \approx 2.5$ will be almost grey. Numerical simulations have shown that mutual aggregate collisions can only produce an aggregate with fractal dimension $d_{\rm f} \approx 2.5$ (Suyama et al. 2008; Wada et al. 2008). Hence, collision-compressed aggregates may produce grey scattered-light colours at near-infrared wavelength. Another possibility is that the aggregate with $d_{\rm f} \approx 2$ has the monomer radius slightly larger than 0.1 μm but not as large as micron size. This can also produce grey colours. The third possibility is the conventional one, that is, compact particles with the radius comparable to the observing wavelength (Fig. B4). Although composite mixture of compact particles and porous aggregates in the same disc may also affect disc colours, this is left for a future task.

6 COMPARISON WITH DISC OBSERVATIONS

Near-infrared observations of protoplanetary discs have shown that most discs show grey colours in both total and polarized intensity (Fukagawa et al. 2010; Avenhaus et al. 2018). Previously, these scattered-light properties are interpreted as the presence of compact grains with the radius comparable to the observing wavelength (see Fig. B4). In this case, it is necessary that dust grain radii at disc surface are adjusted to observing wavelength. One adjusting mechanism could be dust vertical stratification (Duchêne et al. 2004; Pinte et al. 2007). This study provides a new insight into interpretation of discs showing grey colours. We found that large porous dust aggregates can also show marginally grey or slightly blue total intensity. One advantage is that in the case of porous aggregates, their radius is not necessary to adjust to observing wavelength. In addition, large porous dust aggregates are expected to be stirred higher altitude of the discs, they are likely to affect disc scattered light. Therefore, grey discs in total intensity might by explained by large fluffy dust aggregates, although more detail modelling is necessary for each object.

If a disc contains porous dust aggregates, we predict that polarization fraction of disc scattered light should be high. For example, as shown in Fig. 4, porous aggregates with sub-micron monomers produce polarization fraction as high as 65–75 per cent and disc integrated polarization fraction is about 18 per cent at $\lambda = 1.6\,\mu$m at inclination angle $i = 60^\circ$ (see also Table 1).

Spatially resolved polarization fraction map is obtained for several discs, and these observations have revealed that disc scattered light in near-infrared wavelengths is often highly polarized. Polarization fraction of GG Tau and AB Aur discs show polarization fraction as high as 50 per cent at $\lambda = 1\,\mu$m for GG Tau (Silber

Downloaded from https://academic.oup.com/mnras/article-abstract/485/4/4951/5372459 by Bungaku-Bu Library user on 20 May 2020

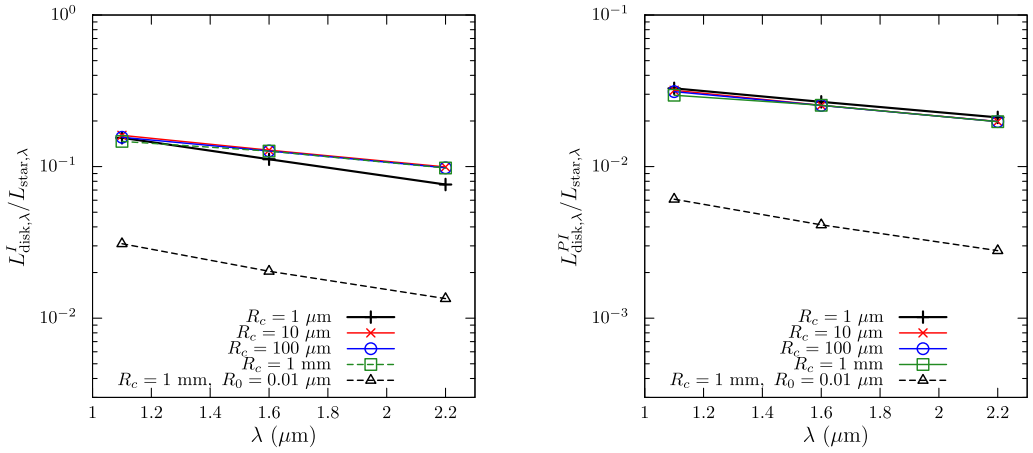

Figure 8. Fractional luminosity of the disc for total intensity (left) and polarized intensity (right).

[t]

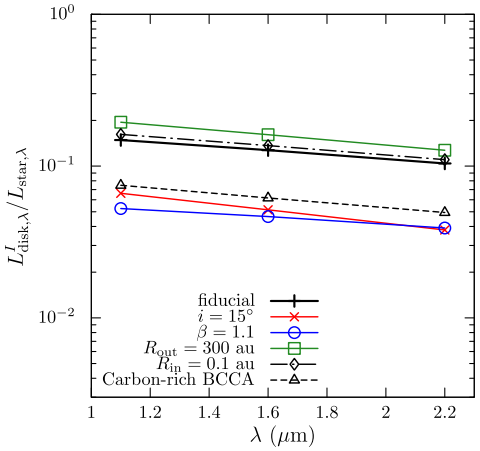

Figure 9. Fractional luminosity for total intensity for various disc and dust composition, where the dust morphology is the BCCA model ($R_c = 4.8\ \mu$m and $R_0 = 0.1\ \mu$m). The fiducial model has the inclination angle $i = 60^\circ$, the flaring index $\beta = 1.25$, the inner and outer radii $R_{\rm in} = 10$ au and $R_{\rm out} = 100$ au, respectively, and the dust composition is astronomical silicate (plus symbol). Each parameter is changed one by one from the fiducial model; the fiducial model, but for $i = 15^\circ$ (cross), for $\beta = 1.1$ (circle), for $R_{\rm out} = 300$ au (square), for $R_{\rm in} = 0.1$ au (diamond), and for carbon-rich BCCA (triangle).

Table 4. Disc scattered-light colour for different disc and dust models.

Dust model	$\eta_{\rm I}$	$\eta_{\rm PI}$
fiducial	−0.51	−0.41
$i = 15^\circ$	−0.80	−0.46
$\beta = 1.1$	−0.43	−0.30
$R_{\rm out} = 300$ au	−0.61	−0.47
$R_{\rm in} = 0.1$ au	−0.55	−0.47
Carbon-rich BCCA	−0.60	−0.66

et al. 2000) and $\lambda = 2\ \mu$m for AB Aur (Perrin et al. 2009). More recently, Itoh et al. (2014) reported polarization fraction of GG Tau is as high as that of Rayleigh scattering function at *H* band; nevertheless, strong forward scattering is also observed at *H* band. For HD 142527, Canovas et al. (2013) derived polarization fraction of 10–25 per cent at *H* band; however, Avenhaus et al. (2014) reported significantly higher polarization fraction for this object (20–45 per cent) at *H* band. Tanii et al. (2012) show that polarization fraction of UX Tau is up to 66 per cent at *H* band. Furthermore, Poteet et al. (2018) have shown that polarization fraction of TW Hya is as high as 63 per cent ± 9 per cent. Thus, scattered light of these spatially resolved objects is highly polarized, and hence these scattered light might be explained by porous dust aggregates models, although both detail modelling for each object and further observational studies to derive polarization fraction are necessary. It should be emphasized that polarization fraction predicted by our porous dust aggregate model is not *very* high compared to disc observations.

Mulders et al. (2013) pointed out that some protoplanetary discs show reddish scattered-light colour in total intensity. For the case of the outer disc of HD 100546, reddish and faint scattered light are observed, and it can be explained by 2.5-μm-sized spherical particles (Mulders et al. 2013). Based on the SED modelling of HD 100546, Mulders et al. (2013) also claimed that the disc scale height is consistent with a particle model of 0.1 μm rather than 2.5 μm for a given turbulent strength and disc gas mass. They suggested a possibility that the presence of *extremely fluffy* dust aggregates containing submicron-sized monomers at the disc surface layer may reconcile this apparent conflict, since such dust aggregate behaves like a small particle in dynamics and like a large particle in light scattering process. However, we found that fluffy aggregates of submicron-sized monomers do not show reddish colour in total intensity. Reddish scattered light is more likely to be observed when the dust aggregates have compact structure (see Figs B4 and 10). Therefore, our results imply that fluffy dust aggregates are not responsible for the scattered-light properties of the outer disc of HD 100546. Our results predict that polarization fraction of HD 100546 should not be high. Quanz et al. (2011) show that integrated polarization fraction of this disc is about 14 per cent. Since average inclination angle of HD 100546 is 46° (Mulders et al. 2013), observed polarization fraction is lower than the prediction of our BCCA model, which shows about 32 per cent at $i = 45^\circ$ (Table 1). This observed polarization fraction is more close to our compact dust aggregate model. Recently, Stolker et al. (2016) derived scattering phase function of this object. The derived phase function increases with increasing scattering angles from intermediate to back scattering angles. This enhanced backward scattering can be seen in phase function of compact dust aggregates (Min et al. 2016), and not

Downloaded from https://academic.oup.com/mnras/article-abstract/485/4/4951/5372459 by Bungaku-Bu Library user on 20 May 2020

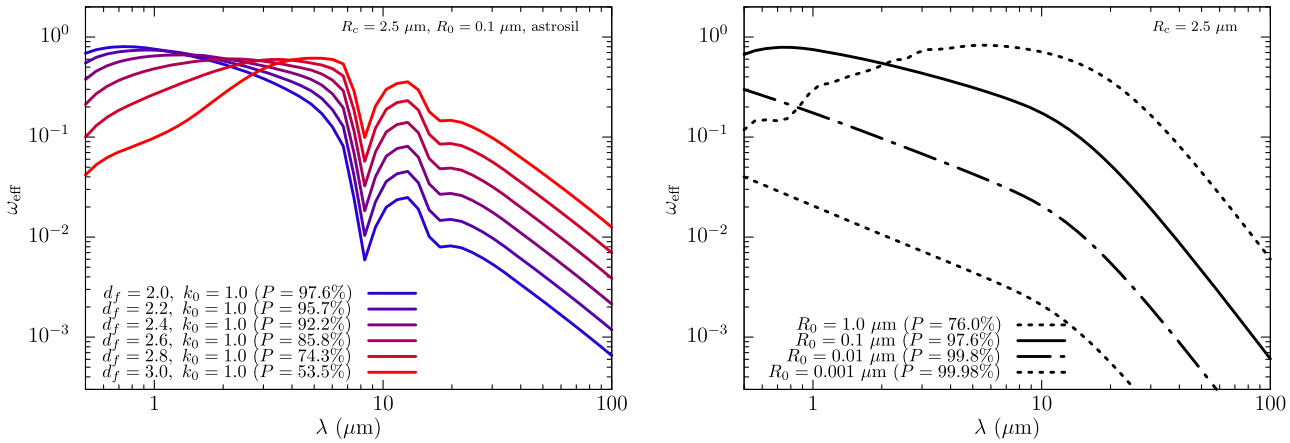

Figure 10. (Left) The effective albedo for different values of $d_{\rm f}$ and k_0, where the characteristic radius and monomer radii are $R_{\rm c} = 2.5\,\mu$m and $R_0 = 0.1\,\mu$m, respectively. Refractive index is astronomical silicate. (Right) The effective albedo of fluffy dust aggregates ($k_0 = 1.0$ and $d_{\rm f} = 2$) of various monomer radii. The characteristic radius is assumed to be 2.5 μm. Refractive index is set as $m = 1.67 + 0.0326i$, which corresponds to those of astronomical silicate at $\lambda = 1.6\,\mu$m.

for fluffy dust aggregate (Paper I, see also Fig. 2). Laboratory experiments also support that large compact particles show the enhanced backscattering (Muñoz et al. 2017). These enhanced backscattering presumably due to the presence of wavelength scale surface roughness of a large compact particle (e.g. Mukai et al. 1982). Thus, phase function of this object is consistent with our implication.

7 CONCLUSION

We have studied how radius and structure of dust aggregates affect observational quantities of protoplanetary discs in near-infrared wavelengths. We have performed radiative transfer calculations of protoplanetary discs taking fluffy dust aggregates into account, where we first treated their optical properties in a proper manner. Furthermore, based on an approximate theory for optical properties of fractal dust aggregates (MMF) (Paper I; Paper II), we have argued scattering properties of fractal dust aggregates. Our primary findings are summarized as follows.

(i) The ratio of an aggregate radius and wavelength can be assessed by the presence of brightness asymmetry in total intensity images. Both porous and compact dust aggregates can produce brightness asymmetry in total intensity when their radii exceed the observing wavelength (Sections 2.3 and 3).

(ii) Polarization fraction of a disc is useful to probe structure of dust aggregates as long as the aggregate radius exceeds observing wavelength (Sections 2.3 and 3). Higher porosity produces higher polarization fraction. We have provided expected integrated polarization fraction for various dust models and disc inclinations (Table 1).

(iii) Porous dust aggregates (BCCAs and BPCAs) large compared to near-infrared wavelengths show marginally grey or slightly blue in total or polarized intensity. Meanwhile, large compact dust aggregates show reddish scattered-light colour in total intensity (Section 4.1).

(iv) For sufficiently large BCCA, the aggregate radius is less sensitive to disc scattered light because of saturation of scattering property (Figs 6 and 7). Even if the radius is increased up to millimetre-size, BCCA containing 0.1-μm-sized monomers is expected to show marginally grey or slightly blue colours (Section 4.2).

(v) Within a parameter range we studied, the disc geometry, inclination angle, and composition seems not to be sensitive to the disc scattered-light colours in near-infrared wavelengths, although these can affect magnitude of fractional luminosity (Section 4.3).

(vi) The effective albedo for aggregate with various fractal dimensions and monomer radius is computed. As fractal dimension or monomer radius increases, wavelength dependence of the effective albedo varies from blue to red at near-infrared wavelengths. BCCA can show reddish colours in near-infrared wavelengths when the monomer is about micron-sized. On the other hand, smaller monomers make BCCA a bluer scatterer in near-infrared wavelength (Section 5).

ACKNOWLEDGEMENTS

We sincerely thank the referee for a thorough and careful reading of the manuscript. R.T. would like to thank Daniel Mackowski and Yasuhiko Okada for the availability of the T-Matrix code with the QMC method. R.T. also thanks Cornelis P. Dullemond for making the `RADMC-3D` code public. R.T. thanks Robert Botet for fruitful discussion. R.T. was supported by a Research Fellowship for Young Scientists from the Japan Society for the Promotion of Science (JSPS) (17J02411).

REFERENCES

Augereau J. C., Lagrange A. M., Mouillet D., Papaloizou J. C. B., Grorod P. A., 1999, A&A, 348, 557
Avenhaus H., Quanz S. P., Schmid H. M., Meyer M. R., Garufi A., Wolf S., Dominik C., 2014, ApJ, 781, 87
Avenhaus H. et al., 2018, ApJ, 863, 44
Bentley M. S. et al., 2016, Nature, 537, 73
Berry M. V., Percival I. C., 1986, Opt. Acta, 33, 577
Blum J., Schräpler R., Davidsson B. J. R., Trigo-Rodríguez J. M., 2006, ApJ, 652, 1768
Bohren C. F., Huffman D. R., 1983, Absorption and scattering of light by small particles, Wiley, New York
Botet R., Rannou P., Cabane M., 1997, Appl. Opt., 36, 8791
Brisset J., Heißelmann D., Kothe S., Weidling R., Blum J., 2017, A&A, 603, A66
Bruggeman D. A. G., 1935 , Ann. Phys., Lpz., 416, 636

Downloaded from https://academic.oup.com/mnras/article-abstract/485/4/4951/5372459 by Bungaku-Bu Library user on 20 May 2020

Canovas H., Ménard F., Hales A., Jordán A., Schreiber M. R., Casassus S., Gledhill T. M., Pinte C., 2013, A&A, 556, A123
Draine B. T., Lee H. M., 1984, ApJ, 285, 89
Duchêne G., McCabe C., Ghez A. M., Macintosh B. A., 2004, ApJ, 606, 969
Dullemond C. P., Natta A., 2003, A&A, 408, 161
Dullemond C. P., Juhasz A., Pohl A., Sereshti F., Shetty R., Peters T., Commercon B., Flock M. 2012, Astrophysics Source Code Library, record ascl:1202.015
Fukagawa M. et al., 2010, PASJ, 62, 347
Fulle M. et al., 2015, ApJ, 802, L12
Fulle M. et al., 2016, MNRAS, 462, S132
Halder P., Deb Roy P., Das H. S., 2018, Icarus, 312, 45
Henning T., Stognienko R., 1996, A&A, 311, 291
Itoh Y. et al., 2014, Res. Astron. Astrophys., 14, 1438–1446
Kataoka A., Tanaka H., Okuzumi S., Wada K., 2013, A&A, 557, L4
Kataoka A., Okuzumi S., Tanaka H., Nomura H., 2014, A&A, 568, A42
Kempf S., Pfalzner S., Henning T. K., 1999, Icarus, 141, 388
Kenyon S. J., Hartmann L., 1987, ApJ, 323, 714
Kimura H., Kolokolova L., Mann I., 2006, A&A, 449, 1243
Kirchschlager F., Wolf S., 2014, A&A, 568, A103
Kolokolova L., Kimura H., Kiselev N., Rosenbush V., 2007, A&A, 463, 1189
Kothe S., Blum J., Weidling R., Güttler C., 2013, Icarus, 225, 75
Laor A., Draine B. T., 1993, ApJ, 402, 441
Long Z. C. et al., 2017, ApJ, 838, 62
Mackowski D. W., Mishchenko M. I., 1996, J. Opt. Soc. Am., 13, 2266
Mannel T., Bentley M. S., Schmied R., Jeszenszky H., Levasseur-Regourd A. C., Romstedt J., Torkar K., 2016, MNRAS, 462, S304
Min M., Hovenier J. W., de Koter A., 2005, A&A, 432, 909
Min M., Kama M., Dominik C., Waters L. B. F. M., 2010, A&A, 509, L6
Min M., Dullemond C. P., Kama M., Dominik C., 2011, Icarus, 212, 416
Min M., Canovas H., Mulders G. D., Keller C. U., 2012, A&A, 537, A75
Min M., Rab C., Woitke P., Dominik C., Ménard F., 2016, A&A, 585, A13
Mukai S., Mukai T., Giese R. H., Weiss K., Zerull R. H., 1982, Moon Planets, 26, 197
Mukai T., Ishimoto H., Kozasa T., Blum J., Greenberg J. M., 1992, A&A, 262, 315
Mulders G. D., Min M., Dominik C., Debes J. H., Schneider G., 2013, A&A, 549, A112
Muñoz O., Moreno F., Vargas-Martín F., Guirado D., Escobar-Cerezo J., Min M., Hovenier J. W., 2017, ApJ, 846, 85
Okada Y., 2008, J. Quant. Spec. Radiat. Transf., 109, 17 19
Okuzumi S., Tanaka H., Kobayashi H., Wada K., 2012, ApJ, 752, 106
Ormel C. W., Spaans M., Tielens A. G. G. M., 2007, A&A, 461, 215
Perrin M. D., Schneider G., Duchene G., Pinte C., Grady C. A., Wisniewski J. P., Hines D. C., 2009, ApJ, 707, L132
Pinte C., Fouchet L., Ménard F., Gonzalez J.-F., Duchêne G., 2007, A&A, 469, 963
Poteet C. A. et al., 2018, ApJ, 860, 115
Quanz S. P., Schmid H. M., Geissler K., Meyer M. R., Henning T., Brandner W., Wolf S., 2011, ApJ, 738, 23
Shen Y., Draine B. T., Johnson E. T., 2008, ApJ, 689, 260
Shen Y., Draine B. T., Johnson E. T., 2009, ApJ, 696, 2126
Silber J., Gledhill T., Duchêne G., Ménard F., 2000, ApJ, 536, L89
Stolker T., Dominik C., Min M., Garufi A., Mulders G. D., Avenhaus H., 2016, A&A, 596, A70
Suyama T., Wada K., Tanaka H., 2008, ApJ, 684, 1310
Tanii R. et al., 2012, PASJ, 64, 124
Tazaki R., Tanaka H., Okuzumi S., Kataoka A., Nomura H., 2016, ApJ, 823, 70 (Paper I)
Tazaki R., Tanaka H., 2018, ApJ, 860, 79 (Paper II)
Wada K., Tanaka H., Suyama T., Kimura H., Yamamoto T., 2008, ApJ, 677, 1296
Wada K., Tanaka H., Suyama T., Kimura H., Yamamoto T., 2011, ApJ, 737, 36
Ysard N., Jones A. P., Demyk K., Boutéraon T., Koehler M., 2018, A&A, 617, A124
Zubko V. G., Mennella V., Colangeli L., Bussoletti E., 1996, MNRAS, 282, 1321

APPENDIX A: COMPARISON BETWEEN APPROXIMATE METHODS

We perform radiative transfer simulation of the BCCA model with approximate methods – modified mean field theory (MMF; Paper II), effective medium theory with Maxwell Garnett mixing rule (EMT; Mukai et al. 1992; Kataoka et al. 2014), and DHS – and then the results are compared to those obtained by TMM.

Fig. A1 shows scattered-light images of the disc at the wavelength of $\lambda = 1.6\,\mu$m and the inclination angle of $i = 60^\circ$, where the dust model is the BCCA model with $N = 1024$ and $R_0 = 0.1\,\mu$m. As shown in Paper II, for this BCCA model, MMF coincides with the mean field theory (MFT) results at $\lambda > 0.85\,\mu$m. Hence, we use MFT instead of MMF.

Fig. A1 clearly shows that MFT reproduces the TMM results, whereas EMT and DHS fail.

First of all, we study the difference of each method in total intensity of the discs (see middle panels in Fig. A1). All methods show the front-back asymmetry. Both MFT and DHS show similar results to the TMM result; however, the EMT result significantly deviates from the TMM result. This is because EMT produces extremely faint backward scattering (Fig. A2, see also fig 5 of Paper I) due to destructive interference of scattered waves. In other words, extremely strong forward scattering predicted by the EMT model means that most of the photons coming from the star are just passing through the particle, and they are not likely to be scattered toward the observer. As a result, when EMT is applied to obtain optical properties of BCCA, the disc scattered light becomes too faint.

Secondly, we study polarization fraction (bottom panels in Fig. A1). Fig. A1 shows that TMM and MFT show almost the same polarization fraction; however, EMT and DHS overestimate and underestimate polarization fraction, respectively (Fig. A3). The low polarization fraction of DHS is due to scattering property of the particle (Fig. A2). The degree of polarization of the BCCA model at wavelength $1.6\,\mu$m shows has a bell-shaped angular profile (almost symmetric with respect to $\theta = 90^\circ$), and maximum degree of polarization is 96 per cent at $\theta = 90^\circ$ (Fig. A2, see also fig. 15 of Paper I). However, the DHS model predicts the degree of polarization is 40 per cent at $\theta = 90^\circ$, which is significantly lower than the TMM result. As a consequence, polarization fraction of DHS becomes lower than that of TMM. The overestimation of polarization fraction of EMT is due to a radiative transfer effect. As shown in Paper I, both EMT and MFT show a similar polarization profile to TMM.[9] Nevertheless, EMT significantly overestimates polarization fraction. As we have mentioned, in the EMT model, large-angle scattering is suppressed by destructive interference, and hence, multiple scattering at the disc surface layer is not likely to occur. Since MFT can reproduce phase function obtained by the TMM correctly (see fig. 5 in Paper I), MFT can mimic the depolarization effect in radiative transfer, whereas EMT fails.

[9]The degree of polarization obtained by MFT is almost the same as that of the RGD theory because phase shift is less than unity for the dust model and wavelength now we concern (see also Paper II).

Downloaded from https://academic.oup.com/mnras/article-abstract/485/4/4951/5372459 by Bungaku-Bu Library user on 20 May 2020

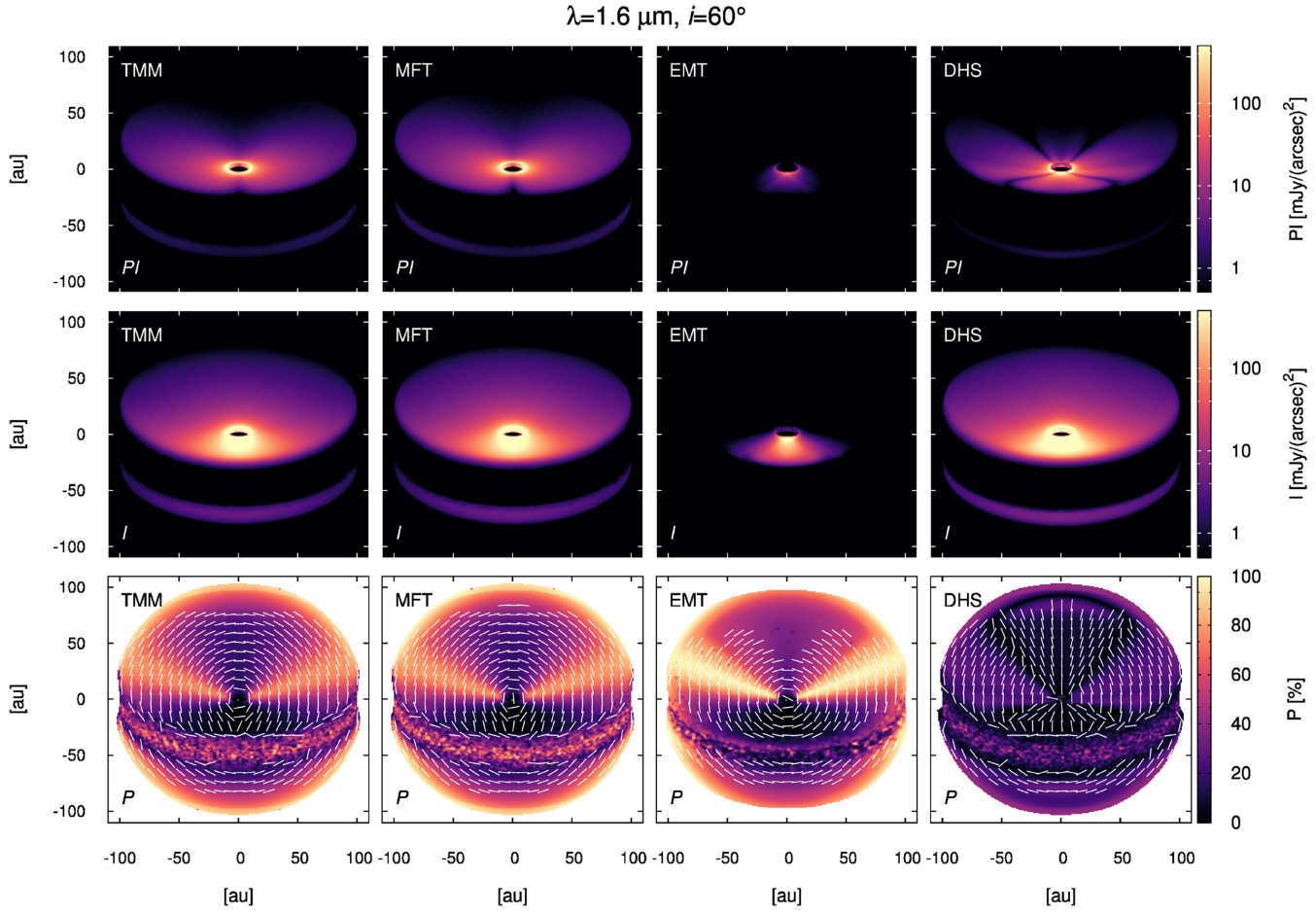

Figure A1. Polarized intensity (top), total intensity (middle), and polarization fraction (bottom). From left to right, TMM, MFT, EMT, and DHS are used. Wavelength is $\lambda = 1.6\,\mu$m and the inclination angle is $i = 60^\circ$. The dust model adopted here is BCCA with $N = 1024$ and $R_0 = 0.1\,\mu$m, corresponding to the characteristic radius $R_c = 4.8\,\mu$m.

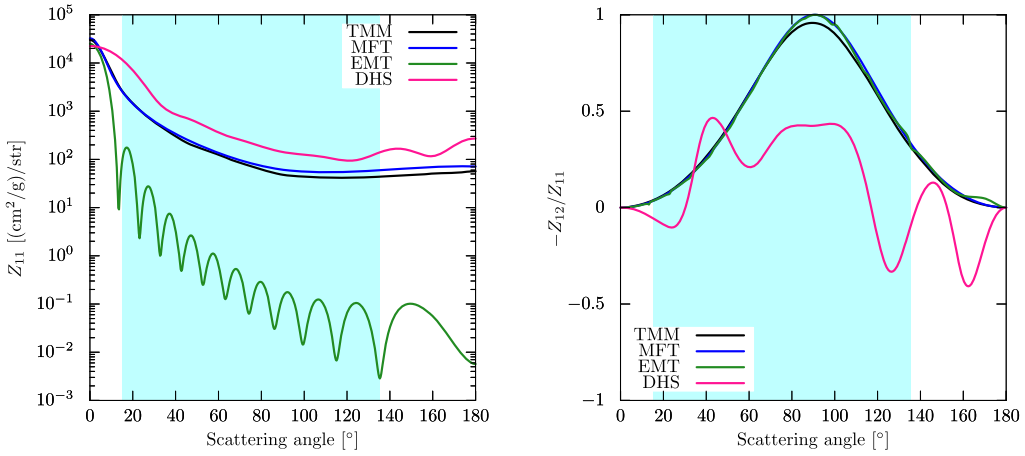

Figure A2. Phase function Z_{11} (left), and the degree of linear polarization $-Z_{12}/Z_{11}$ (right). The dust model is the BCCA model. Black line is the result obtained by TMM method (rigorous numerical method), while others (MFT, EMT, DHS) are those obtained by using the approximate method for optical property calculations. MFT can reproduce the TMM results for both intensity and polarization fraction, whereas EMT and DHS fail. Hatched region indicates a range of scattering angle to be observed for a disc with the flaring index $\beta = 1.25$ and the inclination angle $i = 60^\circ$.

Downloaded from https://academic.oup.com/mnras/article-abstract/485/4/4951/5372459 by Bungaku-Bu Library user on 20 May 2020

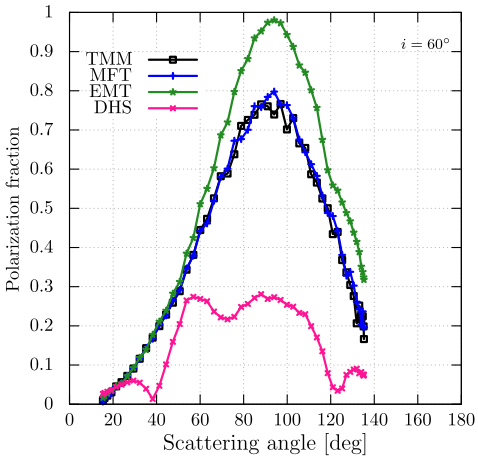

Figure A3. Polarization fraction as a function of scattering angles at $R = 50$ au measured from simulated images in Fig. A1.

Table A1. Disc scattered-light colour for BCCA with different methods.

Method	$\eta_{\rm I}$	$\eta_{\rm PI}$
TMM	− 0.51	− 0.41
MFT	− 0.67	− 0.67
EMT	0.53	0.65
DHS	0.030	0.099

The DHS model shows some slits in the image of polarized intensity. This is because oscillatory behaviour in an angular profile of the degree of polarization originated from resonance of smooth spherical surface. Since the degree of polarization becomes positive and negative in the oscillatory behaviour, polarization vectors in DHS are very different from the TMM results. In the DHS model, optical properties are averaged over the size distribution; nevertheless, the oscillatory behaviour remains. This is mainly because astronomical silicate is less absorbing at infrared wavelengths.

Fig. A4 show scattered-light colour in total intensity and in polarized intensity calculated at inclination angle $i = 60°$ obtained by various approximate methods. Table A1 shows colours of the BCCA model for various solution methods for their optical properties. The MFT model is able to reproduce the TMM results compared to other approximate methods. DHS shows red colour in total intensity. It is also found that once the EMT is used to obtain optical properties of large BCCA, the disc becomes faint and reddish; however, it should be strengthened that this is due to the artefact arising from the use of the Mie theory.

Finally, we show some obtained radiative transfer images for large BCCA studied in Section 4.2. By applying MFT to BCCA with $R_{\rm c} = 1\,\mu$m to 1 mm, we obtain Fig. A5. Because of saturation of scattering properties of BCCA (Figs 6 and 7), scattered-light images of BCCA with various radius look similar (see also Section 4.2).

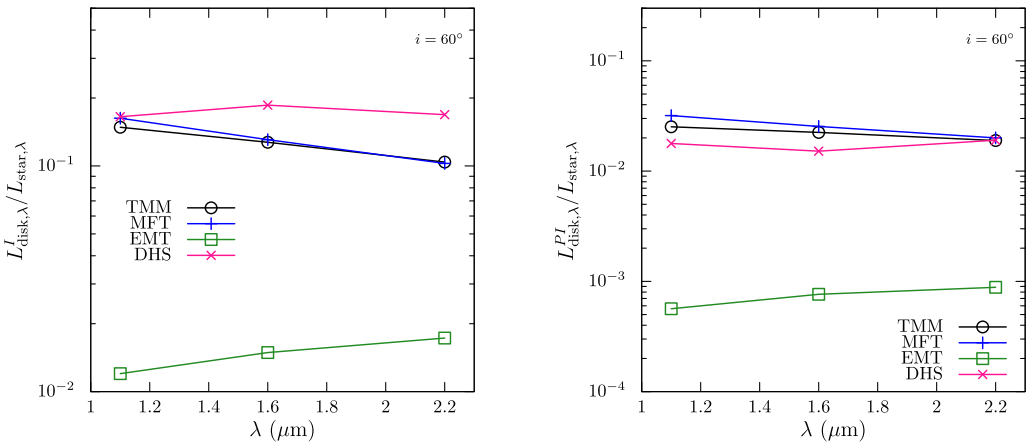

Figure A4. Fractional luminosity of an inclined disc ($i = 60°$) for total intensity (left) and polarized intensity (right).

Downloaded from https://academic.oup.com/mnras/article-abstract/485/4/4951/5372459 by Bungaku-Bu Library user on 20 May 2020

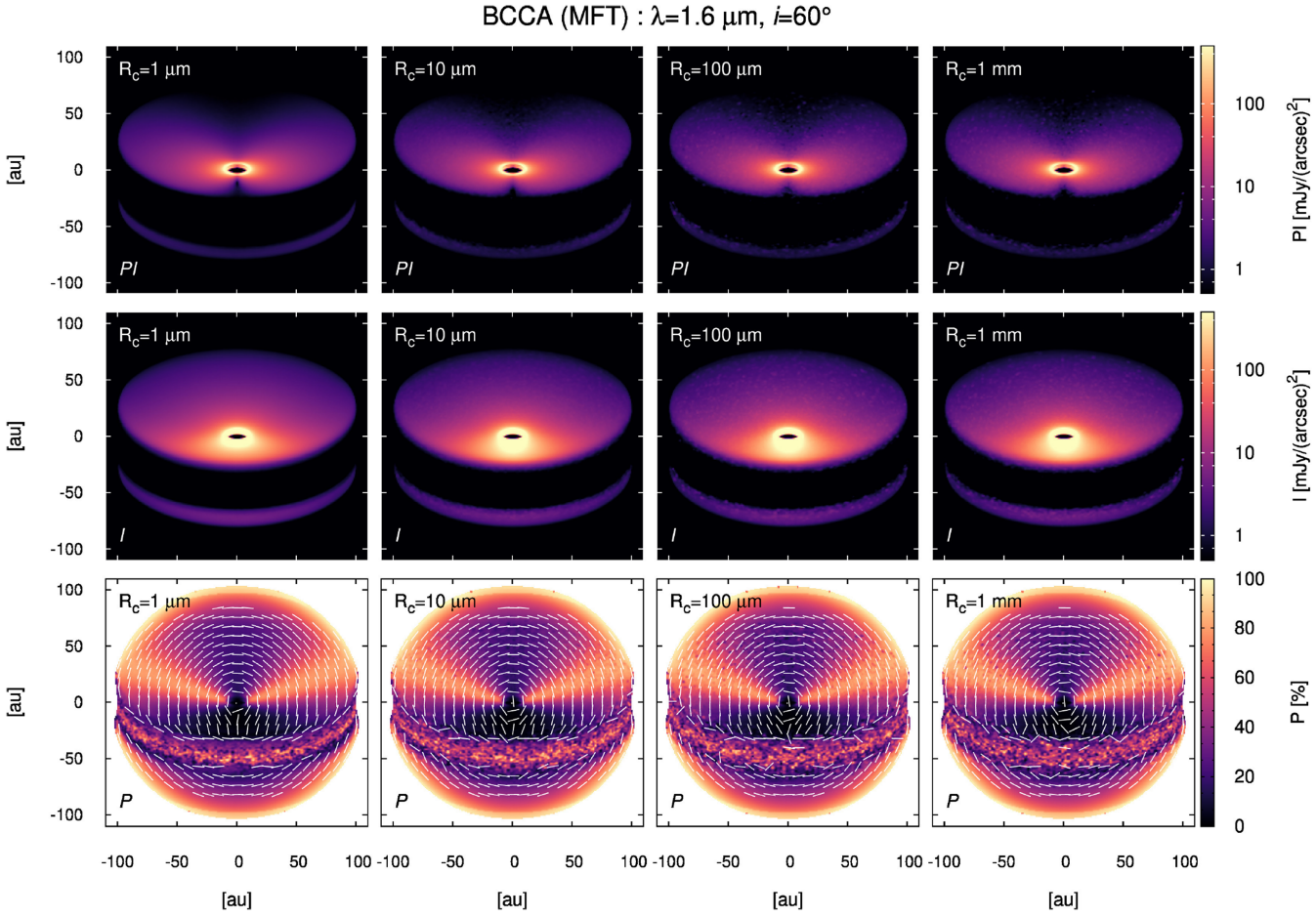

Figure A5. Polarized intensity (top), total intensity (middle), and polarization fraction (bottom). From left to right, scattered-light images of BCCA with $R_c = 1\,\mu$m, $10\,\mu$m, $100\,\mu$m, and 1 mm are shown, respectively, where optical properties of BCCA are computed by using MFT.

APPENDIX B: COMPACT DUST AGGREGATES

Scattered-light images and colours of the compact dust aggregate models with various radii are presented.

B1 *H*-band Images

Fig. B1 shows scattered-light images at $\lambda = 1.6\,\mu$m for the compact dust aggregate models and the single monomer model for comparison. By using the scattered-light mapping, Fig. B3 shows scattered-light intensity and polarization fraction as a function of scattering angle at $R = 50$ au.

First of all, we discuss total intensity. When the aggregate radius is smaller than $\lambda/2\pi$, the disc is faint and shows weak front-back brightness asymmetry. Once the aggregate radius exceeds $\lambda/2\pi$, the disc begins to show front-back brightness asymmetry in total intensity. In addition, when the aggregate radius exceeds 1.0 μm, the disc total scattered light becomes faint with increasing the aggregate radius. This is because scattering phase function of large compact dust aggregate is sharply peaked at forward scattering angles, and then this results in reducing effective single scattering albedo (Dullemond & Natta 2003; Min et al. 2010; Mulders et al. 2013).

Second, we argue polarization fraction. When the radius of compact dust aggregate is 0.1 μm, polarization fraction becomes more than 90 per cent because Rayleigh scattering happens. As the aggregate radius increases, polarization fraction decreases. However, once the aggregate radius exceeds 1.0 μm, polarization fraction increases again as the aggregate radius increases. This is due to the effect of Brewster scattering, which finally brings the degree of polarization to 100 per cent at the Brewster angle (Min et al. 2016) in the limit of sufficiently large grain radius. Based on light scattering simulations of compact dust aggregates, Min et al. (2016) showed that compact dust aggregates do not show high degree of polarization at the Brewster scattering, unlike the prediction of the DHS method. The perfect polarization at the Brewster angle is thought to be arising from the ignorance of the surface roughness of compact dust aggregates in the DHS method (Min et al. 2016), and hence we expect that the realistic compact dust aggregates may not show the increase of polarization fraction at the Brewster angle.

B2 Scattered-light colours

Fig. B4 shows disc scattered-light colour in total intensity and in polarized intensity for the compact dust aggregate models. Table B1 shows colours of compact aggregates for various aggregate radii.

When the radius of the dust aggregate is smaller than the wavelength, the disc is faint and very blue in total intensity. As the radius increases, disc luminosity increases and disc colour becomes grey when the aggregate radius is comparable to the wavelength. Once the aggregate radius exceeds the wavelength, the disc becomes reddish and faint as expected by Mulders et al. (2013).

Downloaded from https://academic.oup.com/mnras/article-abstract/485/4/4951/5372459 by Bungaku-Bu Library user on 20 May 2020

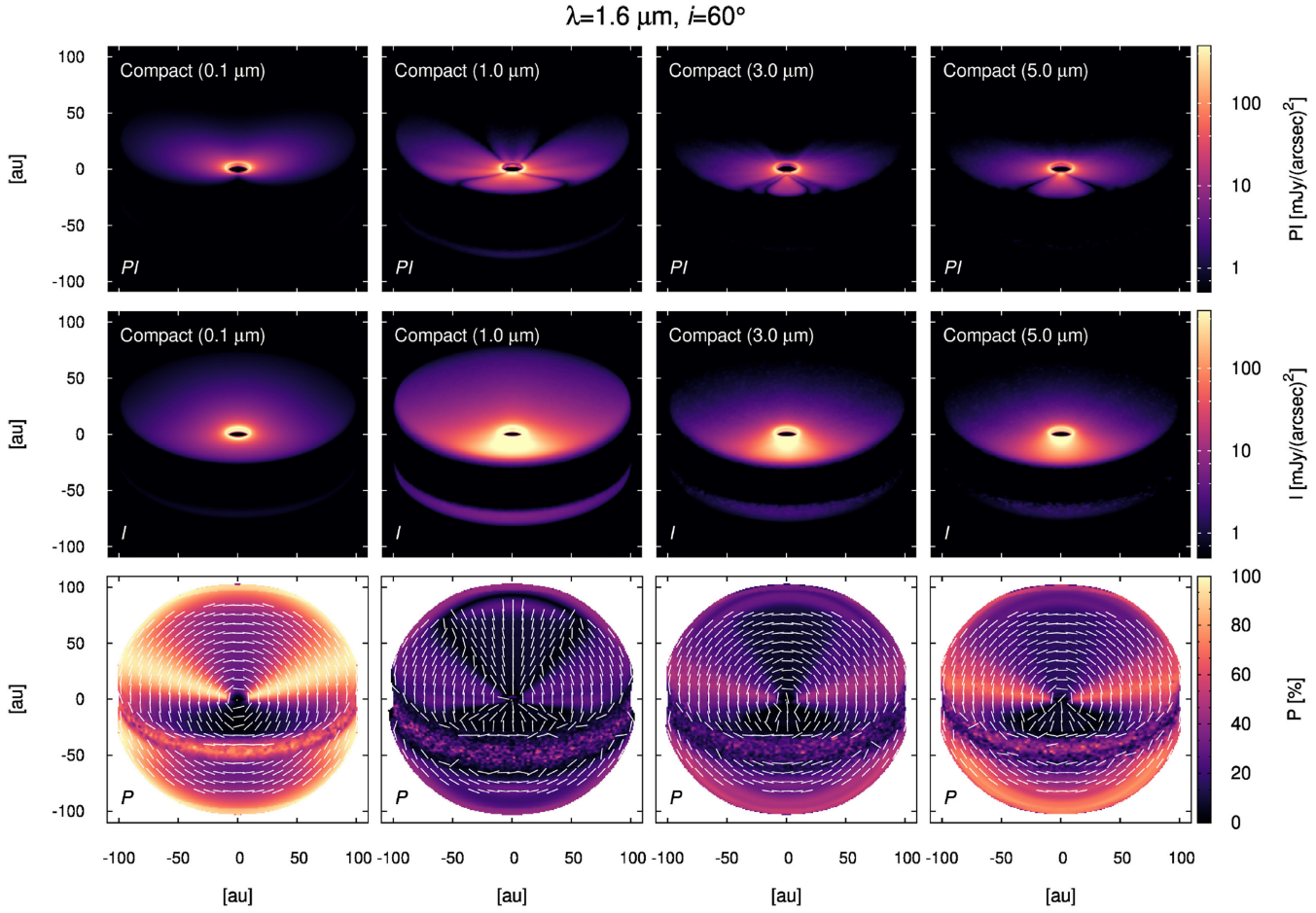

Figure B1. Polarized intensity (top), total intensity (middle), and polarization fraction (bottom). Scattered-light images of the single monomer model (leftmost) and the compact dust aggregate models (right three columns).

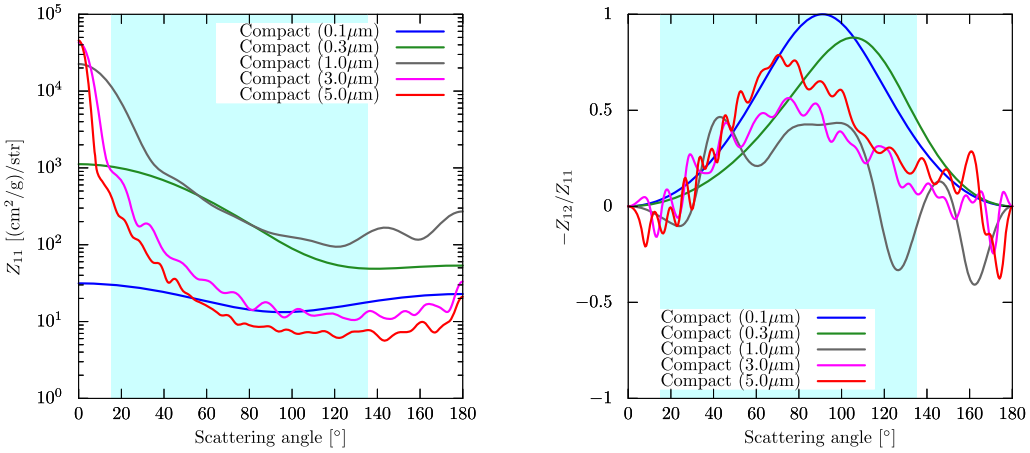

Figure B2. Phase function Z_{11} (left) and the degree of linear polarization $-Z_{12}/Z_{11}$ (right). Optical properties of compact dust aggregates are obtained by DHS. Hatched region indicates a range of scattering angle to be observed for a disc with the flaring index $\beta = 1.25$ and the inclination angle $i = 60°$.

Next, we discuss polarized intensity. Similar to the case of total intensity, small dust aggregates show blue colours in polarized intensity. When the aggregate radius is comparable to the wavelength, polarized intensity is reddish. For the large aggregate radius, polarized intensity shows grey colours; however, it is partially due to Brewster scattering. Hence, if we consider the effect of surface roughness of compact dust aggregates, polarized intensity colours might be more reddish, although more detailed computations are necessary.

Downloaded from https://academic.oup.com/mnras/article-abstract/485/4/4951/5372459 by Bungaku-Bu Library user on 20 May 2020

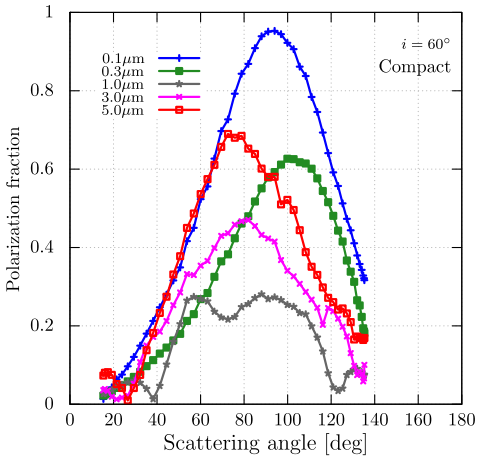

Figure B3. Polarization fraction as a function of scattering angles at $R = 50$ au measured from simulated images in Fig. B1.

Table B1. Disc scattered-lightcolour for compact aggregates with various radii.

Dust model	$\eta_{\rm I}$	$\eta_{\rm PI}$
0.1 μm	− 2.4	− 2.3
0.3 μm	− 0.93	2.6
1.0 μm	0.030	0.099
3.0 μm	0.84	0.60
5.0 μm	0.70	0.11

APPENDIX C: THE ASYMMETRY PARAMETER OF SUFFICIENTLY LARGE BCCA

The asymmetry parameter can be expressed as

$$g = \frac{2\pi}{k^2 C_{\rm sca,agg}} \int_{-1}^{1} \mu S_{11,\rm agg}(\mu) {\rm d}\mu, \tag{C1}$$

where $C_{\rm sca,\,agg}$ is the scattering cross-section of the dust aggregate, k is the wavenumber, $S_{11,\,\rm agg}$ is a (1,1) element of scattering matrix of dust aggregates, and $\mu = \cos\theta$, where θ is the scattering angle. Using the single scattering assumption, a scattering matrix element of dust aggregates can be written by

$$S_{11,\rm agg}(\mu) = N^2 S_{11,\rm mono}(\mu)\mathcal{S}(q), \tag{C2}$$

where the magnitude of scattering vector $q = 2k\sin(\theta/2)$ and $\mathcal{S}(q)$ is the structure factor (Paper I). When $qR_g \gg 1$ and $d_{\rm f} = 2$, we can approximately decompose the scattering phase function of fluffy dust aggregates by the sum of coherent and incoherent contribution:

$$S_{11,\rm agg}(\mu) = S_{11,\rm agg}^{\rm coherent} + S_{11,\rm agg}^{\rm incoherent}, \tag{C3}$$

$$S_{11,\rm agg}^{\rm coherent} \simeq N^2 S_{11,\rm mono}(\mu)\delta(\mu - 1), \tag{C4}$$

$$S_{11,\rm agg}^{\rm incoherent} \simeq N S_{11,\rm mono}(\mu)[(qR_0)^{-2} + 1], \tag{C5}$$

where we have used equation (29) of Paper I. Using equations (C1 and C3) and $qR_0 \ll 1$, we obtain

$$g \simeq \frac{2\pi N}{k^2 C_{\rm sca,agg}} \int_{-1}^{1} \mu (qR_0)^{-2} S_{11,\rm mono}(\mu){\rm d}\mu, \tag{C6}$$

Since scattering cross-section is approximately proportional to k^2 (Berry & Percival 1986) and $S_{11,\,\rm mono} \propto k^6$ (Rayleigh scattering) (Bohren & Huffman 1983), the asymmetry parameter g becomes wavelength independent. Therefore, sufficiently large dust aggregates ($qR_{\rm g} \gg 1$) with $d_{\rm f} = 2$ containing small monomers ($qR_0 \ll 1$) yield wavelength-independent asymmetry parameter.

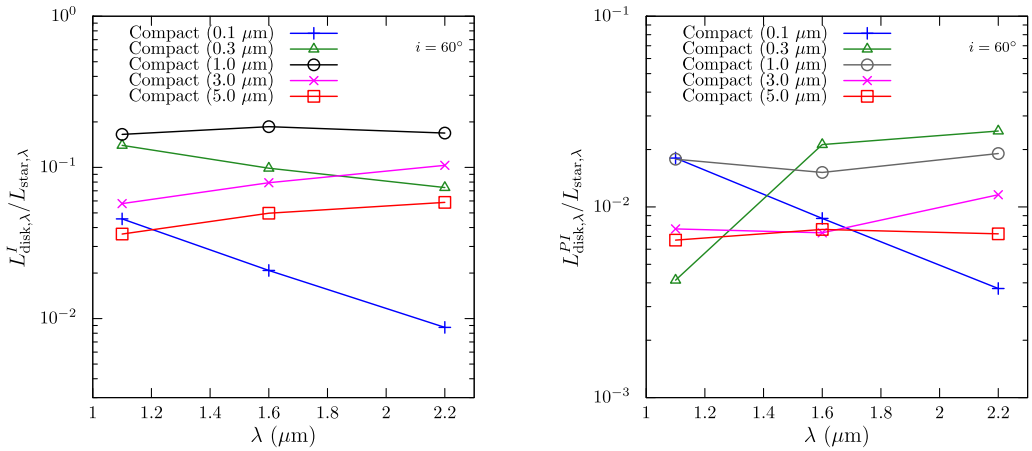

Figure B4. Scattered-light colours in total intensity (left) and in polarized intensity (right) of the compact dust aggregate models. The disc inclination is assumed to be $i = 60°$. Once the size parameter of the grain exceeds unity, the disc scattered light becomes faint and red as the grain radius increases.

This paper has been typeset from a TEX/LATEX file prepared by the author.

Downloaded from https://academic.oup.com/mnras/article-abstract/485/4/4951/5372459 by Bungaku-Bu Library user on 20 May 2020